Measurement of net electric charge and dipole moment of dust aggregates in a complex plasma

Razieh Yousefi,[*] Allen B. Davis, Jorge Carmona-Reyes,[†] Lorin S. Matthews,[‡] and Truell W. Hyde[§]
CASPER, Physics Department, Baylor University, Waco, Texas 76798-7316, USA
(Received 11 May 2014; revised manuscript received 6 August 2014; published 2 September 2014)

Understanding the agglomeration of dust particles in complex plasmas requires knowledge of basic properties such as the net electrostatic charge and dipole moment of the dust. In this study, dust aggregates are formed from gold-coated mono-disperse spherical melamine-formaldehyde monomers in a radiofrequency (rf) argon discharge plasma. The behavior of observed dust aggregates is analyzed both by studying the particle trajectories and by employing computer models examining three-dimensional structures of aggregates and their interactions and rotations as induced by torques arising from their dipole moments. These allow the basic characteristics of the dust aggregates, such as the electrostatic charge and dipole moment, as well as the external electric field, to be determined. It is shown that the experimental results support the predicted values from computer models for aggregates in these environments.

DOI: 10.1103/PhysRevE.90.033101 PACS number(s): 52.70.Ds, 52.58.Qv, 52.70.Nc

I. INTRODUCTION

The agglomeration of micron- and submicron-sized particles is a fundamental process that occurs over a range of environments. Dust plays a key role in the evolution of molecular clouds and the early stage of star and planet formation. The processes governing the evolution of the system are tied to the properties of the dust grains, such as the size distribution and porosity (fluffiness) of the aggregates [1,2]. The formation of ice particles on dust grains in Earth's upper atmosphere gives rise to unusual phenomena such as noctilucent clouds and localized electron depletions ("biteouts") associated with these clouds [3]. These ice particles also reflect and absorb energy, influencing atmospheric dynamics [4]. Dust is also readily found in magnetic confinement fusion devices, which has consequences for the safety of fusion reactors as well as their operation and performance [5]. Additionally, the coagulation of dust in plasma, following gas-phase nucleation, is a source of contamination in semiconductor processing [6,7].

In many of the environments mentioned above the dust is charged, either by being immersed in a radiative or plasma environment or through triboelectric charging. While the microphysics of the coagulation process is fundamental to all of these areas, it is not yet well understood. One of the reasons for this is the fact that knowledge of the basic properties of dust particles is required to better understand and explain these phenomena. The particle electrostatic charge and the dipole moment are two of the most important parameters that help to define dusty plasma since they determine both the particle interactions with themselves as well as with the plasma particles and existing electromagnetic fields.

Grains in a plasma environment often attain charges sufficiently large that they are equally affected by local electrical and gravitational fields [8,9]. One method for calculating the charge of isolated dust grains in a Maxwellian plasma is orbital-motion-limited (OML) theory, which has been applied to spherical dust grains [10,11], cylindrical dust particles [12], and less symmetric isolated particles using a nonspherical probe [13]. The charge on nonisolated dust grains, where interactions between dust particles is taken into account, has also been investigated theoretically [14]. Measurement of the charge on dust grains in laboratory experiments has also been performed for both isolated [15] and nonisolated dust grains [16]. For most conditions, experimental results agree fairly well with theoretical predictions.

Dust grains in astrophysical and laboratory plasmas are not necessarily spherically symmetric; the grains are typically elongated [17,18] or aggregates consisting of many small subunits [19]. It has been shown that aggregates in both laboratory and astrophysical environments tend to acquire more charge compared to spherical grains of the same mass due to their porous structure [20–23]. A fluffy aggregate, consisting of many spherical monomers, has charge distributed over its irregular surface, which leads to a nonzero dipole moment.

The electric charge and the dipole moment of aggregates play a very important role in the coagulation process. An opposite charge polarity can lead to enhanced coagulation as a result of mutual electrostatic attraction [3,24,25]. However, grains that are in a plasma environment usually obtain the same charge polarity. The coagulation of like-charged grains, while less efficient than the coagulation of oppositely charged grains, may be enhanced if charged grains are assumed to have a dipole moment due to the arrangement of charge over the grain surface [26–29]. These charge-dipole interactions have been inferred from experiment [25,30,31] and modeled numerically [24,32–34].

It is evident that any proper explanation of agglomeration of dust particles requires a fundamental understanding of the electrostatic charge and dipole moment of dust aggregates. In numerical studies, the electric charge and the dipole moment of aggregates in a plasma environment have been calculated using modified OML theory [23,32,34] and the interaction between two charged grains modeled by calculating the torques and accelerations due to the charged aggregates or external electric fields [24,32,33]. However, a direct study of both the electrostatic charge and the dipole of dust particles in laboratory plasmas has not yet been performed. In this study, we present a model for these complex plasma environments,

[*]Raziyeh_Yousefi@baylor.edu
[†]Jorge_Carmona_Reyes@baylor.edu
[‡]Lorin_Matthews@baylor.edu
[§]Truell_Hyde@baylor.edu

where dust aggregates formed in a laboratory plasma and their basic properties are investigated. These results are then compared with an existing numerical model.

II. EXPERIMENT

In this work, all complex plasma experiments are performed in a modified Gaseous Electronics Conference (GEC) rf reference cell. The vacuum chamber has two electrodes, a lower cylindrical electrode driven at a frequency of 13.56 MHz and a hollow cylindrical upper electrode, which is grounded. Single gold-coated melamine formaldehyde (mf) spheres with a mass of $(6.10 \pm 0.09) \times 10^{-13}$ kg are introduced into the argon plasma from a shaker located above the upper electrode. The dust particles are confined inside a 1 in. open-ended glass box placed on the lower electrode. See [35] for complete description of the experimental setup. The plasma is typically maintained at a rf peak-to-peak voltage of 80 V and a pressure of 500 mTorr, allowing the particles to form a stable cloud within the box. Using the same method as reported in [36] for creating the aggregates, the particles are accelerated by triggering self-excited dust density waves by rapidly decreasing the pressure to 50 mTorr. After several minutes, the pressure is returned to the initial level, and aggregates consisting of up to ≈20 monomers are observed. Aggregates are back-lit using a 500 W flood lamp and imaged using a CMOS monochromatic high-speed camera (1024 FASTCAM Photron) at 3000 fps. To ensure that aggregates form within the focal plane of the camera and lens assembly, the glass box is placed off-center on the lower electrode, closer to the window where the camera is mounted. The recorded field of view spans an area of 717 μm × 829 μm with a resolution of 1.4 μm/pixel. The aggregates and their interactions are sampled randomly as the particles move through the focal plane of the camera, which is less than 500 μm thick as compared to the 2.25 cm box side length.

In the experiment, observed aggregates tend to be linear and elongated. Individual aggregates are often observed to rotate about the vertical z axis, with a rotation period of approximately a few hundredths of a second. A representative sample of the aggregates observed is shown in Fig. 1. Aggregate rotation allows three-dimensional models to be reconstructed, as illustrated in Fig. 2. Spherical monomers are used to match the projected two-dimensional (2D) orientation of an aggregate over several frames as it moves and rotates, with the final positions of the monomers adjusted so that each monomer is connected at at least one point. Interacting aggregate pairs exhibit rotation induced by their charge-dipole interactions, as shown in Fig. 3.

III. NUMERICAL MODEL

Two numerical codes are used to model the charging and interaction of the aggregates. The interaction between two charged grains, including rotations induced by torques due to the charge dipole moments, is modeled using the AGGREGATE_BUILDER code [32–34]. The electric charge and dipole moment are calculated using OML_LOS, which is based on OML (orbital-motion-limited) theory modified to determine the open lines of sight (LOS) to points on the surface of the aggregate [33,34]. Electrons and ions in the plasma

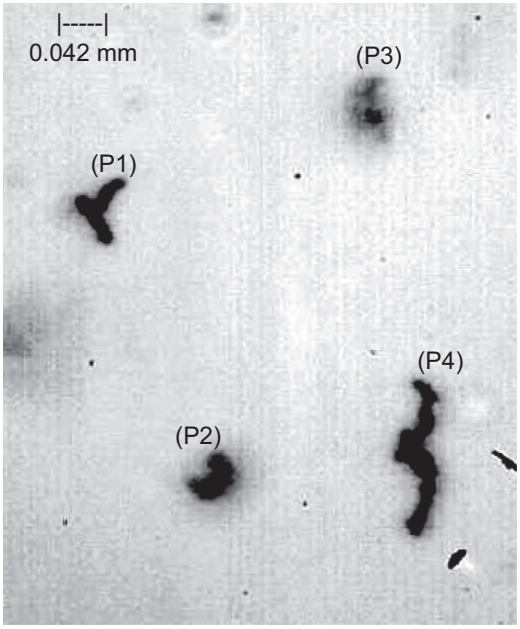

FIG. 1. A representative single frame of rotating aggregates showing four particles. Rotation of P1–P3 about the vertical axis was observed, while P4 was moving from right to left without any rotation, probably due to its small horizontal electric dipole moment.

are incident to the surface along the open LOS, yielding a charge distribution over the aggregate surface. Calculations are made assuming an electron temperature $T_e = 23\,400$ K (≈ 2 eV), ion temperature $T_i = 298$ K, and $n_e = n_i = 1 \times 10^{14}$ m^{-3}, where n_e is the number density of electrons and n_i is the number density of ions. The total charge is found by summing the charge on the surface of each monomer, while the dipole moment is calculated from $\vec{p} = \Sigma_i q_i \vec{r}_i$, where q_i is the total charge on the ith monomer and $\vec{r}_i$ is the radial position of the ith monomer in the center-of-mass coordinate system of each aggregate. Note that the values derived from (OML_LOS) code are sensitive to the number of monomers and their exact arrangements used to build up the 3D structure of the aggregates. Figure 4 shows a 3D model of aggregate P5 (shown in Fig. 3) modified by displacing or removing one or two of the monomers at different positions to illustrate the resulting change in charge and electric dipole moment, listed in Table I.

IV. ANALYSIS

In the experiment, the rate of change of the center-of-mass velocity $\vec{v}$ for particles with mass m and charge q was calculated using the equation of motion including gravity, $\vec{F}_G$, gas drag, $\vec{F}_D$, and the electrostatic force, $\vec{F}_E$, acting on the particle,

$$m\frac{d\vec{v}}{dt} = \vec{F}_G + \vec{F}_D + \vec{F}_E. \quad (1)$$

For weakly ionized plasmas, we consider only neutral gas drag since it dominates the ion drag [37]. The neutral drag force is given by the Epstein formula [38]

$$\vec{F}_D = -\beta m \vec{v}, \quad (2)$$

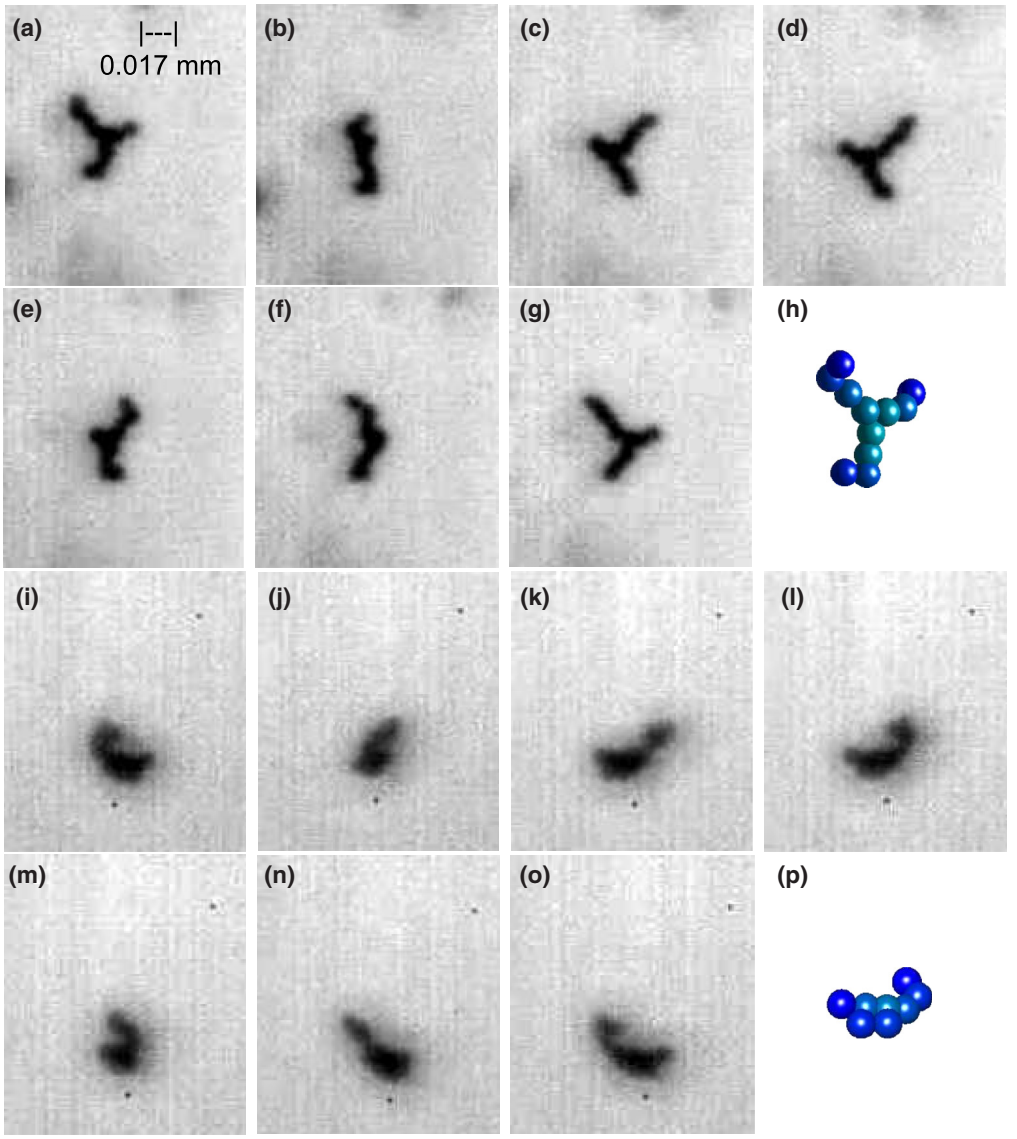

FIG. 2. (Color online) (a)–(g) Sequence of images showing the complete rotation of cluster P1 from Fig. 1 consisting of eleven 8.93 μm gold-coated mf particles ($\Delta t = 0.0167$ s), and (h) its reconstructed 3D model. (i)–(o) P2 from Fig. 1 consisting of eight particles ($\Delta t = 0.0117$ s), and (p) its reconstructed 3D model. Spatial scaling is the same for all the subimages.

where β is the damping coefficient, which was determined experimentally for a single mf sphere. Using the same method as described in [39], a VERDI Ti:sapphire continuous-wave (cw) laser was used to perturb a dust grain, which oscillated about its equilibrium position. Fits to the damped oscillatory motion were used to find $\beta = 9.8 \pm 0.9$ s^{-1}. Since β is proportional to the cross-sectional area of spherical particles, the drag coefficient for larger aggregates is found by scaling β by the projected (2D) cross-sectional area.

The electrostatic force arises from the interaction of dust particle with charge q with the electric field from other dust grains, $\vec{E}_{\rm int}$, the vertical electric field in the sheath above

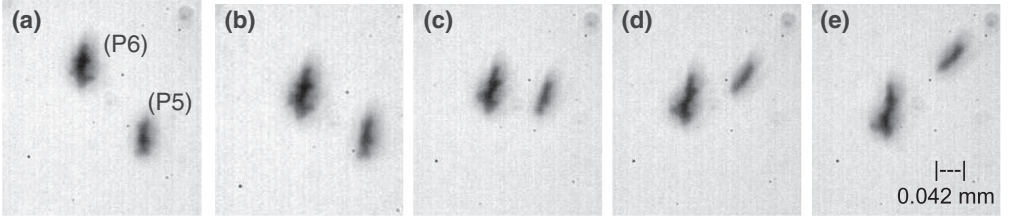

FIG. 3. A sequence of images showing a sample interaction between two charged dust particles (P5) and (P6). P5 begins in the bottom right and P6 begins in the top left ($\Delta t = 0.001$ s).

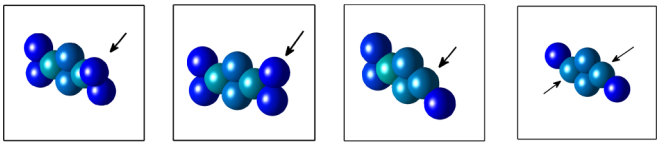

(a) (b) (c) (d)

FIG. 4. (Color online) Proposed structure of aggregate P5 consisting of different numbers of monomers. (a,b) Eight monomers, with the location of the displaced monomer indicated by an arrow, (c) seven monomers, and (d) six monomers, with the locations of the removed monomers indicated by arrows.

the lower electrode, $\vec{E}_z$, and a confining electric field in the horizontal direction arising from the walls of the box, $\vec{E}_r$,

$$\vec{F}_E = q(\vec{E}_{\rm int} + \vec{E}_z + \vec{E}_r). \tag{3}$$

Assuming a screened Coulomb potential around each dust particle, the electric field produced by a charged particle is

$$\vec{E}_{\rm int} = \frac{q}{4\pi\epsilon_0}\left\{\frac{\vec{r}}{r^2} + \frac{\vec{r}}{r\lambda}\right\}\frac{e^{-\frac{r}{\lambda}}}{r}, \tag{4}$$

where r is the radial distance from the center of the particle and λ is the screening length, which is estimated to be equal to the electron Debye length, $\lambda_D = (kT_e\epsilon_0/n_e e^2)^{1/2}$, due to the high mobility of electrons in the plasma sheath where dust particles are levitating [40–42]. $\vec{E}_z$, the vertical electric field, is taken to be unknown in all the calculations, and $\vec{E}_r$ is the confining electric field due to the Yukawa potential inside the box arising from the negative charges on the walls of the box [43].

The rotation of a particle is driven by the total torque acting on the dust particle. The angular acceleration α of the particle is given by

$$\frac{d\vec{Ł}}{dt} = I\vec{\alpha} = \vec{\tau}_E + \vec{\tau}_D, \tag{5}$$

where $\vec{Ł}$ is the angular momentum, I is the moment of inertia of the aggregate about the axis of rotation, $\vec{\tau}_E = \vec{p} \times \vec{E}$ is the torque due to the electric field including $\vec{E}_{\rm int}$, $\vec{E}_z$, and $\vec{E}_r$, and $\vec{\tau}_D = \sum_i \vec{r}_i \times \vec{F}_D$ is the torque due to the drag force, with $\vec{r}_i$ being the perpendicular distance from the center of each monomer to the vertical axis passing through the center of mass, about which the aggregate is rotating.

TABLE I. Electric charge q, total dipole moment $|\vec{p}|$, and projection of dipole moment in the image plane, $|\vec{p}_r|$, of aggregates in Fig. 4 derived from OML_LOS.

Aggregate	q (10^{-14} C)	$\lvert\vec{p}\rvert$ (10^{-20} C m)	$\lvert\vec{p}_r\rvert$ (10^{-20} C m)
(a)	−0.58	0.37	0.37
(b)	−0.58	0.24	0.23
(c)	−0.55	0.89	0.79
(d)	−0.52	0.30	0.23

V. RESULTS

For rotating aggregates, a sequence of 500 image frames was analyzed using ImageJ [44]. A number of aggregates, almost fixed in place, spinning about the vertical z axis with a nearly constant angular velocity, were observed (Fig. 1). Two of the particles, P1 and P2, which are in focus, were examined using the 3D models shown in Figs. 2(h) and 2(p). The total charge on these rotating aggregates was estimated numerically using the OML_LOS code to be $q_1 = -0.82 \times 10^{-14}$ C and $q_2 = -0.59 \times 10^{-14}$ C, respectively. Since these aggregates show little vertical or horizontal translational motion, the gravitational force acting on the particles is assumed to be balanced by the electrostatic force due to the vertical electric field. Using this fact, the magnitude of the vertical electric field, corresponding to the position of each aggregate, is estimated to be $E_{z1} = 0.80 \times 10^4$ V/m and $E_{z2} = 0.81 \times 10^4$ V/m. The resulting electric field gradient is consistent with the results reported in [45]. The Debye length of the plasma is estimated to be about 0.1 mm using the values of T_e, T_i, n_e, and n_i given in Sec. III. The minimum distance between the rotating aggregates in the 2D images is measured to be ∼0.3 mm, which is several times larger than the estimated Debye length. Therefore, it is reasonable to assume that $\vec{E}_{\rm int}$ is negligible between the particles.

Noninteracting aggregates are only observed to rotate about a vertical axis passing through the center of mass. The gravitational force, acting at the center of mass, and the vertical electrostatic force, acting at the "center of charge," exert opposing forces and an aligning torque [31] with any rotation about a horizontal axis damped by gas drag. The force exerted by the horizontal electric field causes a rotation about the vertical axis, and damping from gas drag causes an aggregate to spin at a constant rate. The rotational angular velocity is measured by determining the number of frames (± frame) for a spinning aggregate to return to its initial orientation averaged over four complete rotations. Previous experiments with the same experimental conditions estimated the magnitude of the horizontal electric field to be $|\vec{E}_r| =$ 100 V/m [43]. Using this value in Eq. (5), and calculating the drag force as described for the 3D model, allows the magnitude of the electric dipole moment in the horizontal plane to be calculated, resulting in values of $|\vec{p}_{1r}| = 3.15 \times 10^{-19}$ C m and $|\vec{p}_{2r}| = 0.31 \times 10^{-19}$ C m with 25% uncertainty due to a combined uncertainty in E_r, drag force, and angular velocity. These values are in very good agreement with the values predicted by OML_LOS, $|\vec{p}_{1r}| = 3.1 \times 10^{-19}$ C m and $|\vec{p}_{2r}| = 0.29 \times 10^{-19}$ C m. It is interesting to note that the value of the horizontal electric dipole moment for P4, which is observed to have no rotation during the measured time frame, is predicted to be $|\vec{p}_{1r}| = 0.09 \times 10^{-19}$ C m by OML_LOS. The small value of the horizontal electric dipole moment could be one reason for the lack of rotation.

For the interacting aggregate pairs, a 30-frame sequence of images, showing a short interaction between two charged dust particles, P5 and P6, was analyzed using ImageJ. As shown in Fig. 3, P5 enters the frame from the lower right and P6 enters the frame from the upper left. As they approach one another, their paths are deflected. P5's rotation about an axis perpendicular to the image plane is considerable. A

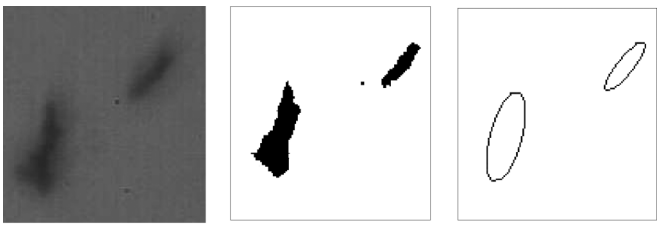

(a)Raw image (b)Binary image (c)Analyzed image

FIG. 5. Illustration of image processing. (a) A raw image loaded into ImageJ. (b) A binary image after setting a pixel value threshold in the program for the image shown in (a). (c) Image analysis by fitting ellipses snugly around the detected aggregates in (b) through the "analyze particle" function.

pixel value threshold was set in the program to convert the gray-scale image into a binary image [Fig. 4(b)]. The "analyze particles" function in ImageJ was then used to fit ellipses snugly around the particles detected as shown in Fig. 5(c) to determine the center-of-mass coordinates and orientations, and the angle between the ellipse's major axis to the horizontal axis for all the particles in each frame. Figure 6 shows the center-of-mass positions $X_{\text{c.m.}}$ and $Y_{\text{c.m.}}$ ($\pm 5.6\ \mu$m) for both particles as they change over time overlaid on four frames from the movie, with their orientation as a function of time shown in Fig. 7. A polynomial function was fit to the X and Y positions as a function of time for each particle, with velocity and acceleration of the particles derived by differentiating these equations [46].

The two vector-component equations from Eq. (1) for the two particles gives the following set of equations:

$$\ddot{x}_5 = -\beta\dot{x}_5 + \frac{q_5 q_6}{4\pi\epsilon_0 m_5}\left\{\frac{1}{r^2}+\frac{1}{r\lambda}\right\}\frac{e^{-\frac{r}{\lambda}}}{r}x_{56} + \frac{q_5 E_r}{m_5},$$

$$\ddot{y}_5 = -\beta\dot{y}_5 + \frac{q_5 q_6}{4\pi\epsilon_0 m_5}\left\{\frac{1}{r^2}+\frac{1}{r\lambda}\right\}\frac{e^{-\frac{r}{\lambda}}}{r}y_{56} + \frac{q_5 E_z}{m_5} - g,$$

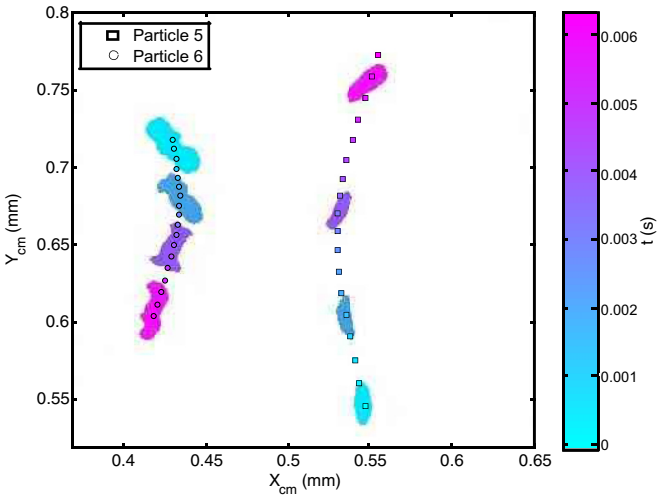

FIG. 6. (Color online) Time evolution of the X and Y components of center-of-mass position for two interacting particles, P5 and P6, superposed on four frames from Fig. 3, with color indicating the time.

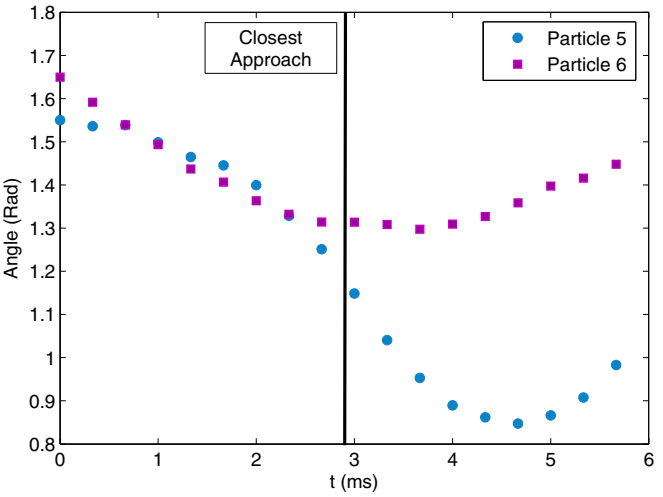

FIG. 7. (Color online) Orientation angle vs time for P5 and P6, with the solid line showing the time of closest approach.

$$\ddot{x}_6 = -\beta\dot{x}_6 + \frac{q_5 q_6}{4\pi\epsilon_0 m_6}\left\{\frac{1}{r^2}+\frac{1}{r\lambda}\right\}\frac{e^{-\frac{r}{\lambda}}}{r}x_{65} + \frac{q_6 E_r}{m_6},$$

$$\ddot{y}_6 = -\beta\dot{y}_6 + \frac{q_5 q_6}{4\pi\epsilon_0 m_6}\left\{\frac{1}{r^2}+\frac{1}{r\lambda}\right\}\frac{e^{-\frac{r}{\lambda}}}{r}y_{65} + \frac{q_5 E_z}{m_6} - g, \quad (6)$$

where x_i and y_i are x and y components of the position of the ith particle, $x_{ij} = x_i - x_j$ and $y_{ij} = y_i - y_j$. The particle's positions, velocities, and accelerations were calculated at the point of closest approach using eight frames of the interaction centered around this time. Substituting these values, along with E_r, into Eq. (6) results in three independent equations:

$$\begin{aligned} 16.3\times10^{-29}q_5q_6 + 20.5\times10^{-18}q_5E_z &= -10.3,\\ 7.3\times10^{-29}q_5q_6 - 10.2\times10^{-18}q_6E_z &= 9.6,\\ q_5q_6 &= 0.4\times10^{-28}, \end{aligned} \quad (7)$$

with three unknown variables: q_5, q_6, and $\vec{E}_z$, where q_5 is the net charge on P5 and q_6 is the net charge on P6. Solving these equations yields $q_5 = -0.48\times10^{-14}$ C ($\pm20\%$), $q_6 = -0.83\times10^{-14}$ C ($\pm17\%$), and $|\vec{E}_z| = 1.11\times10^4$ V/m ($\pm25\%$) in the downward direction.

The electric dipole moments of the dust grains are then calculated from the particles' changing orientations during the interaction. The angular acceleration of each particle was calculated from the orientation, as shown in Fig. 7. Using the values of charge and external electric field found in the previous step, and substituting these values into Eq. (5), the electric dipole moments for each of the dust grains were found to be $|\vec{p}_5| = 0.3\times10^{-20}$ C m and $|\vec{p}_6| = 2.8\times10^{-20}$ C m with an estimated uncertainty of $\pm$ 20%.

Using reconstructed 3D models of P5 consisting of eight monomers, Fig. 4(a), and P6 consisting of 16 monomers in OML_LOS, charges and electric dipole moments of aggregates were calculated as $q_5 = -0.58\times10^{-14}$ C and $q_2 = -0.83\times10^{-14}$ C with corresponding components of dipole moments $|\vec{p}_5| = 0.37\times10^{-20}$ C m and $|\vec{p}_6| = 2.7\times10^{-20}$ C m. These values are in good agreement with the values derived from experiment. The minor differences seen are assumed to arise from the sensitivity of the OML_LOS code to the number of

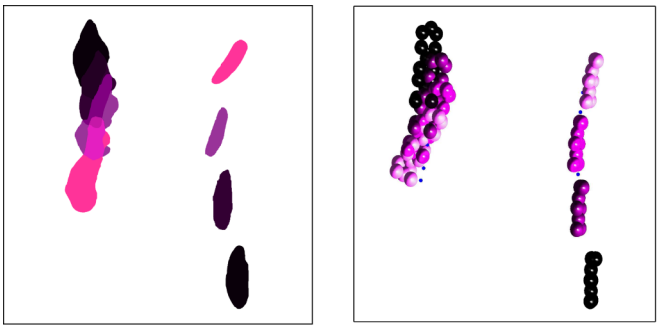

(a) (b)

FIG. 8. (Color online) A superposition of four frames showing the interactions between two aggregates from (a) experimental data with a similar color of aggregates in each frame, and (b) simulation using AGGREGATE_BUILDER code with a similar color of aggregates at each time step. Not all monomers are visible.

monomers and their exact orientation in the constructed 3D aggregates.

The accuracy of the derived values is tested by modeling the dynamics of the interaction in AGGREGATE_BUILDER. Figure 8 compares the observed and the modeled interaction where charges and electric dipoles are those predicted by OML_LOS, using the model for P5 shown in Fig. 4(a). The trajectory and orientation of the modeled aggregates is quite similar to the observed interaction with a small deviation in rotation of aggregates, which could be a result of a change in the magnitude of the charge and the dipole moment of the aggregates as they move within the sheath of the plasma, while these parameters are taken to be constant in the simulation. The forces arising from the external electric fields are quite small compared to the screened Coulomb interaction between the aggregates, and they have a small impact on the particles' trajectories; the dynamics are quite sensitive to the interacting particles' charges and electric dipole moments as well as their initial positions, velocities, and orientations. In Fig. 9, the trajectories and orientations found using the models for P5 depicted in Figs. 4(b)–4(d) are shown for comparison. A smaller dipole moment due to the displacement of a single monomer [Fig. 4(b)] (though within the error bounds of the experimental value) results in an under-rotation of P5 [Fig. 9(a)]. Removing a monomer entirely [Fig. 4(c)] increases the charge-to-mass ratio of P5, but not enough that the trajectory is strongly affected. However, the large dipole moment results in an over-rotation of P5 [Fig. 9(b)]. Removing two monomers [Fig. 4(a)] makes the charge-to-mass ratio small enough that the grain's trajectory deviates substantially from the observed motion.

VI. CONCLUSIONS

Aggregates were formed from gold-coated spherical melamine-formaldehyde monomers in a rf argon discharge plasma. The electrostatic charges and dipole moments of these aggregates were determined through analysis of the extracted particle trajectories and rotations and compared to the output of the numerical models. The excellent agreement between experiment and simulation validates the choice of underlying

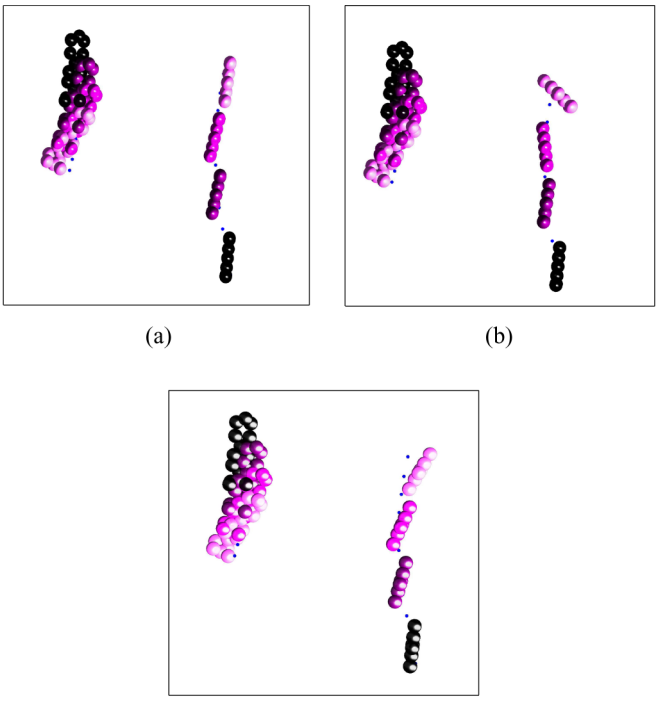

(a) (b) (c)

FIG. 9. (Color online) A superposition of four frames from AGGREGATE_BUILDER code with a similar color of aggregates at each time, showing the interaction of P6 with (a)–(c) the corresponding aggregate in Figs. 4(b), 4(c), and 4(d), respectively.

assumptions. For the numerical models, these include the simplifying assumptions that ion and electron trajectories only impact the aggregate surface along open lines of sight and stick at the point of impact, and that rotations of charged grains are induced by charge-dipole interactions. In deriving values from experiment, assumptions made were neglecting the ion drag force, considering a screened Coulomb interaction between charged particles in order to calculate the force between them, and ignoring the gradient in E_z and E_r during the time of interaction for interacting pair particles.

Previous experiments have observed particle dynamics, which have been attributed to dipole interactions. The electrostatic charges and dipole moments of spherical dielectric particles, dispersed in air passing through a nonuniform electric field, were experimentally measured in [47] by studying the particles' trajectories. In [31], levitated nonspherical (rodlike) particles in the sheath were investigated experimentally, and the magnitude of charge on these particles was numerically calculated considering the charge on a rod immersed in homogeneous ion flow, with the charge monopole, dipole, and quadrupole moments used to explain the observed behavior [29]. In [30], an order-of-magnitude calculation of the dipole moment of a large aggregate with an irregular shape (clump) consisting of N monomers was estimated by modeling the electrostatic force between the clump and a single monomer as a dipole-dipole force, assuming the clump was composed of N monomers identical to the isolated monomer, with a certain fraction of the dipole moments aligned to give an overall dipole moment.

This experimental study analyzes irregular aggregates consisting of spherical monomers, which quantify the dipole moment of individual aggregates. These measurements of the electrostatic charges and dipole moments are of importance in understanding the aggregation process in dynamic simulations studying dust agglomeration where the charge and the electric dipole moment play a very important role and determining the evolution of the grain-sized distribution.

ACKNOWLEDGMENTS

This work is supported by the National Science Foundation under Grants No. 0847127, No. 002637, and No. 1262031.

[1] A. Chokshi, A. G. G. M. Tielens, and D. Hollenbach, Astrophys. J. **407**, 806 (1993).
[2] C. W. Ormel, D. Paszum, C. Dominik, and A. G. G. M. Tielens, Astronomy and Astrophysics **502**, 845 (2009).
[3] G. C. Reid, Geophys. Res. Lett. **24**, 1095 (1997).
[4] S. Shimizu *et al.*, J. Geophys. Res. **115**, D18205 (2010).
[5] J. Winter, Phys. Plasmas **7**, 3862 (2000).
[6] A. Bouchoule and L. Boufendi, Plasma Sources Sci. Technol. **2**, 204 (1993).
[7] L. Boufendi and A. Bouchoule, Plasma Sources Sci. Technol. **3**, 262 (1994).
[8] D. A. Mendis, H. L. F. Houpis, and J. R. Hill, J. Geophys. Res. **87**, 3449 (1982).
[9] D. A. Mendis, J. R. Hill, and H. L. F. Houpis, J. Geophys. Res. **88**, A929 (1983).
[10] *Electric Probes in Plasma Diagnostic Techniques*, edited by F. F. Chen, R. H. Huddlestone, and S. L. Leonard (Academic, New York, 1965), Chap. 4.
[11] J. E. Allen, Phys. Scr. **45**, 497 (1992).
[12] E. C. Whipple, Rep. Prog. Phys. **44**, 1197 (1981).
[13] J. G. Laframboise and L. W. Parker, Phys. Fluids **16**, 629 (1973).
[14] M. S. Barnes, J. H. Keller, J. C. Forster, J. A. O'Neill, and D. K. Coultas, Phys. Rev. Lett. **68**, 313 (1992).
[15] B. Walch, M. Horanyi, and S. Robertson, IEEE Trans. Plasma Sci. **22**, 97 (1994).
[16] A. Barkan, N. D'Angelo, and R. L. Merlino, Phys. Rev. Lett. **73**, 3093 (1994).
[17] U. Mohideen, H. U. Rahman, M. A. Smith, M. Rosenberg, and D. A. Mendis, Phys. Rev. Lett. **81**, 349 (1998).
[18] M. Harwit, *Astrophysical Concepts* (Springer-Verlag, New York, 1988), p. 405.
[19] J. M. Greenberg and J. I. Hage, Astrophys. J. **361**, 260 (1990).
[20] R. Wiese, V. Sushkov, H. Kersten, V. R. Ikkurthi, R. Schneider, and R. Hippler, New J. Phys. **12**, 033036 (2010).
[21] M. Ilgner, Astron. Astrophys. **538**, A124 (2012).
[22] S. Okuzumi, H. Tanaka, T. Takeuchi, and M. Sakagami, Astrophys. J. **731**, 96 (2011).
[23] Q. Ma, L. S. Matthews, V. Land, and T. Hyde, Astrophys. J. **763**, 77 (2013).
[24] L. S. Matthews and T. W. Hyde, IEEE Trans. Plasma Sci. **32**, 586 (2004).
[25] U. Konopka *et al.*, New J. Phys. **7**, 227 (2005).
[26] G. Lapenta, Phys. Rev. Lett. **75**, 4409 (1995).
[27] G. Lapenta, Phys. Plasmas **6**, 1442 (1999).
[28] J. Abrahamson and J. R. Marshall, J. Electrostat. **55**, 43 (2002).
[29] A. V. Ivlev, A. G. Khrapak, S. A. Khrapak, B. M. Annaratone, G. Morfill, and K. Yoshino, Phys. Rev. E **68**, 026403 (2003).
[30] J. R. Marshall, T. B. Sauke, and J. N. Cuzzi, Geophys. Res. Lett. **32**, L11202 (2005).
[31] B. M. Annaratone *et al.*, Phys. Rev. E **63**, 036406 (2001).
[32] L. S. Matthews, R. L. Hayes, M. S. Freed, and T. Hyde, IEEE Trans. Plasma. Sci. **35**, 260 (2007).
[33] L. S. Matthews and T. W. Hyde, IEEE Trans. Plasma Sci. **36**, 310 (2008).
[34] L. S. Matthews, V. Land, and T. W. Hyde, Astrophys. J. **744**, 8 (2012).
[35] J. Kong, T. W. Hyde, L. Matthews, K. Qiao, Z. Zhang, and A. Douglass, Phys. Rev. E **84**, 016411 (2011).
[36] C. Du, H. M. Thomas, A. V. Ivlev, U. Konopka, and G. E. Morfil, Phys. Plasmas **17**, 113710 (2010).
[37] S. Khrapak and G. Morfill, Contrib. Plasma Phys. **49**, 148 (2009).
[38] P. Epstein, Phys. Rev. **23**, 710 (1924).
[39] J. Kong, T. W. Hyde, B. Harris, K. Qiao, and J. C. Reyes, IEEE Trans. Plasma Sci. **37**, 1620 (2009).
[40] K. U. Riemann, J. Phys. D **24**, 493 (1991).
[41] Z. Zhang, K. Qiao, J. Kong, L. Matthews, and T. Hyde, Phys. Rev. E **82**, 036401 (2010).
[42] S. V. Vladimirov and M. Nambu, Phys. Rev. E **52**, R2172 (1995).
[43] T. W. Hyde, J. Kong, and L. S. Matthews, Phys. Rev. E **87**, 053106 (2013).
[44] http://rsbweb.nih.gov/ij/
[45] A. Douglass, V. Land, K. Qiao, L. S. Matthews, and T. Hyde, Phys. Plasmas **19**, 013707 (2012).
[46] Z. Zhang, K. Qiao, J. Kong, L. Matthews, and T. Hyde, Phys. Rev. E **82**, 036401 (2010).
[47] P. Bagga, J. Abrahamson, and J. Marshall, Adv. Powder Technol. **20**, 234 (2009).